



# OGLE-2016-BLG-1227L: A Wide-separation Planet from a Very Short-timescale Microlensing Event

Cheongho Han<sup>1</sup> , Andrzej Udalski<sup>2,18</sup>, Andrew Gould<sup>3,4,19</sup>  
(Leading Authors),

Michael D. Albrow<sup>5</sup> , Sun-Ju Chung<sup>6,7</sup> , Kyu-Ha Hwang<sup>6</sup> , Youn Kil Jung<sup>6</sup>, Chung-Uk Lee<sup>6,19</sup>, Yoon-Hyun Ryu<sup>6</sup> ,  
In-Gu Shin<sup>6</sup> , Yossi Shvartzvald<sup>8</sup> , Jennifer C. Yee<sup>9</sup> , Weicheng Zang<sup>10</sup> , Sang-Mok Cha<sup>6,11</sup>, Dong-Jin Kim<sup>6</sup>,  
Hyoun-Woo Kim<sup>6</sup>, Seung-Lee Kim<sup>6,7</sup>, Dong-Joo Lee<sup>6</sup>, Yongseok Lee<sup>6,11</sup>, Byeong-Gon Park<sup>6,7</sup>, Richard W. Pogge<sup>4</sup> ,  
M. James Jee<sup>12,13</sup>, Doeon Kim<sup>1</sup>, Chun-Hwey Kim<sup>14</sup> , Woong-Tae Kim<sup>15</sup>

(The KMTNet Collaboration),

and

Przemek Mróz<sup>2,16</sup>, Michał K. Szymański<sup>2</sup>, Jan Skowron<sup>2</sup> , Radek Poleski<sup>2,4</sup>, Igor Soszyński<sup>2</sup>, Paweł Pietrukowicz<sup>2</sup> ,  
Szymon Kozłowski<sup>2</sup>, and Krzysztof Ulaczyk<sup>17</sup>

(The OGLE Collaboration)

<sup>1</sup> Department of Physics, Chungbuk National University, Cheongju 28644, Republic of Korea; [cheongho@astroph.chungbuk.ac.kr](mailto:cheongho@astroph.chungbuk.ac.kr)

<sup>2</sup> Warsaw University Observatory, Al. Ujazdowskie 4, 00-478 Warszawa, Poland

<sup>3</sup> Max Planck Institute for Astronomy, Königstuhl 17, D-69117 Heidelberg, Germany

<sup>4</sup> Department of Astronomy, Ohio State University, 140 W. 18th Avenue, Columbus, OH 43210, USA

<sup>5</sup> University of Canterbury, Department of Physics and Astronomy, Private Bag 4800, Christchurch 8020, New Zealand

<sup>6</sup> Korea Astronomy and Space Science Institute, Daejeon 34055, Republic of Korea

<sup>7</sup> Korea University of Science and Technology, 217 Gajeong-ro, Yuseong-gu, Daejeon, 34113, Republic of Korea

<sup>8</sup> Department of Particle Physics and Astrophysics, Weizmann Institute of Science, Rehovot 76100, Israel

<sup>9</sup> Center for Astrophysics|Harvard & Smithsonian 60 Garden Street, Cambridge, MA 02138, USA

<sup>10</sup> Department of Astronomy and Tsinghua Centre for Astrophysics, Tsinghua University, Beijing 100084, People's Republic of China

<sup>11</sup> School of Space Research, Kyung Hee University, Yongin, Gyeonggi 17104, Republic of Korea

<sup>12</sup> Yonsei University, Department of Astronomy, Seoul, Republic of Korea

<sup>13</sup> Department of Physics, University of California, Davis, California, USA

<sup>14</sup> Department of Astronomy & Space Science, Chungbuk National University, Cheongju 28644, Republic of Korea

<sup>15</sup> Department of Physics & Astronomy, Seoul National University, Seoul 08826, Republic of Korea

<sup>16</sup> Division of Physics, Mathematics, and Astronomy, California Institute of Technology, Pasadena, CA 91125, USA

<sup>17</sup> Department of Physics, University of Warwick, Gibbet Hill Road, Coventry, CV4 7AL, UK

Received 2019 November 26; revised 2020 January 8; accepted 2020 January 9; published 2020 February 6

## Abstract

We present the analysis of the microlensing event OGLE-2016-BLG-1227. The light curve of this short-duration event appears to be a single-lens event affected by severe finite-source effects. Analysis of the light curve based on a single-lens single-source (1L1S) model yields very small values of the event timescale,  $t_E \sim 3.5$  days, and the angular Einstein radius,  $\theta_E \sim 0.009$  mas, making the lens a candidate of a free-floating planet. Close inspection reveals that the 1L1S solution leaves small residuals with an amplitude of  $\Delta I \lesssim 0.03$  mag. We find that the residuals are explained by the existence of an additional widely separated heavier lens component, indicating that the lens is a wide-separation planetary system rather than a free-floating planet. From Bayesian analysis, it is estimated that the planet has a mass of  $M_p = 0.79^{+1.30}_{-0.39} M_J$  and it is orbiting a low-mass host star with a mass of  $M_{\text{host}} = 0.10^{+0.17}_{-0.05} M_\odot$  located with a projected separation of  $a_\perp = 3.4^{+2.1}_{-1.0}$  au. The planetary system is located in the Galactic bulge with a line-of-sight separation from the source star of  $D_{\text{LS}} = 1.21^{+0.96}_{-0.63}$  kpc. The event shows that there is a range of deviations in the signatures of host stars for apparently isolated planetary lensing events and that it is possible to identify a host even when a deviation is subtle.

*Unified Astronomy Thesaurus concepts:* [Gravitational lensing \(670\)](#); [Gravitational microlensing exoplanet detection \(2147\)](#)

## 1. Introduction

Although most microlensing planets are detected through the channel of a short-term perturbation to the standard lensing light curve of the planet host (Mao & Paczyński 1991; Gould & Loeb 1992), a fraction of planets can be detected through the channel of an isolated lensing event produced by the gravity of the planet itself (Bennett & Rhie 2002; Han et al. 2004). The

latter channel is important because it provides a unique method to probe free-floating planets (FFPs) that may have been ejected from the planetary systems in which they formed or have not been gravitationally bound to any host star before.

The most important characteristics of an FFP lensing event is its short timescale. This is because the event timescale  $t_E$  is related to the angular Einstein radius  $\theta_E$  and the relative lens-source proper motion  $\mu$  by  $t_E = \theta_E / \mu$ , and the angular Einstein

<sup>18</sup> OGLE Collaboration.

<sup>19</sup> KMTNet Collaboration.

radius is proportional to the square root of the lens mass  $M$ , i.e.,

$$\theta_E = (\kappa M \pi_{\text{rel}})^{1/2}, \quad \pi_{\text{rel}} = \text{au} \left( \frac{1}{D_L} - \frac{1}{D_S} \right). \quad (1)$$

Here  $\kappa = 4G/(c^2 \text{au})$ ,  $\pi_{\text{rel}}$  represents the relative lens-source parallax, and  $D_L$  and  $D_S$  denote the distances to the lens and source, respectively. For FFP events, the chance to exhibit deformed lensing light curves caused by severe finite-source effects is high. The deformation can occur when the angular source radius  $\theta_*$  is comparable to  $\theta_E$  for an FFP event, in which case the light curve is very likely to be affected by severe finite-source effects. Recently, three candidates of FFPs were reported by Mróz et al. (2018, 2019) from the analyses of the lensing events with these characteristics.

However, even when an event is both very short and exhibits strong finite-source effects, the lens cannot be securely identified as an FFP. First, it is always possible that the small value of  $\theta_E$  derives from a small  $\pi_{\text{rel}}$  rather than small lens mass  $M$ . See Equation (1). This issue can only be resolved for individual FFP candidates by measuring the microlens parallax  $\pi_E \equiv \pi_{\text{rel}}/\theta_E$ , using, e.g., a satellite in solar orbit (Refsdal 1966) or a so-called terrestrial parallax (Gould 1997; Gould et al. 2009). Nevertheless, from an ensemble of  $\theta_E$  measurements (even without corresponding  $\pi_E$  measurements), one can statistically constrain the properties of the FFP population. However, there is a second fundamental problem that has the potential to corrupt such a statistical sample, namely that a wide-separation planet can also produce a lensing light curve with similar characteristics, masquerading as an FFP. Therefore, it is important to distinguish the two populations of events produced by FFPs and wide-separation planets in order to draw statistically meaningful conclusions about the properties and frequency of both bound and unbound planets.

Han & Kang (2003) pointed out that an important fraction of isolated short-timescale events produced by wide-separation planets can be distinguished from those produced by FFPs by detecting the signatures of host stars in the lensing light curves.<sup>20</sup> The signatures arise due to the planetary caustic induced by the binarity of the planet–host system. For a binary lens composed of a planet and a host, there exist two sets of caustics. One set of caustics is located close to the host (central caustic) and the other caustic (planetary caustic) is located at a distance of  $s_c = s - 1/s$  from the host. Here  $s$  represents the projected planet–host separation normalized to  $\theta_E$ . The planetary caustic of a wide-separation planet forms a closed curve with four cusps. The full width along the star–planet axis,  $\Delta\xi_c$ , and the height normal to the star–planet axis,  $\Delta\eta_c$ , of the caustic are

$$\Delta\xi_c = \frac{4q^{1/2}}{s\sqrt{s^2 - 1}}; \quad \Delta\eta_c = \frac{4q^{1/2}}{s\sqrt{s^2 + 1}} \quad (2)$$

respectively (Han 2006a). For a wide-separation planet with  $s \gg 1$ , the planetary caustic is located close to the planet, i.e.,  $s_c \rightarrow s$ , and both  $\Delta\xi_c$  and  $\Delta\eta_c$  approach  $4q^{1/2}s^{-2}$ , forming an

asteroid-shape caustic. The caustic size rapidly shrinks with the increase of the planet–host separation, i.e.,  $\Delta\xi_c \sim \Delta\eta_c \propto s^{-2}$ . As the caustic becomes smaller, the signature of the host star diminishes with the increasing finite-source effects.

In this paper, we present the analysis of the lensing event OGLE-2016-BLG-1227. The light curve of the event appears to be approximated by a short-timescale single-lens single-source (1L1S) model with severe finite-source effects, making the lens a candidate FFP. From the close inspection of the light curve, it is found that the 1L1S solution leaves small residuals. We inspect the origin of the residuals to check the existence of a widely separated heavier lens component, i.e., host of the planet.

We organize the paper as follows. In Section 2, we describe the observations of the lensing event and the data obtained from these observations. In Section 3, we present the analysis of the event based on the 1L1S interpretation. In Section 4, we inspect the possible existence of a widely separated host of the planet by conducting a binary-lens (2L1S) analysis. In Section 5, we estimate the angular Einstein radius by determining the dereddened color and brightness of the source star. In Section 6, we conduct a Bayesian analysis of the event to determine the physical lens parameters including the mass and location of the lens system. We summarize the results and conclude in Section 7.

## 2. Observation and Data

The lensing event OGLE-2016-BLG-1227 occurred on a star located toward the Galactic bulge field. The equatorial coordinates of the lensed star (source) are (R.A., decl.)<sub>J2000</sub> = (17 : 42 : 23.31, − 33 : 45 : 35.2), which correspond to the galactic coordinates ( $l, b$ ) = (−4°47′, −1°94′). The source of the event is a bright giant with a baseline magnitude of  $I_{\text{base}} = 16.89$  from the calibrated Optical Gravitational Lensing Experiment (OGLE) photometric maps.

The lensing event was first discovered by the OGLE (Udalski et al. 2015) survey, and the discovery was notified to the microlensing community on 2016 June 29. The OGLE survey was conducted utilizing the 1.3 m telescope located at the Las Campanas Observatory in Chile. The telescope is equipped with a camera, which consists of 32 2k × 4k chips, yielding a 1.4 deg<sup>2</sup> field of view. The OGLE images were obtained mostly in the  $I$  band and some images were taken in the  $V$  band for the source color measurement.

The event was also located in the field toward which the Korea Microlensing Telescope Network survey (KMTNet; Kim et al. 2016) was monitoring. The KMTNet survey was conducted using the three identical 1.6 m telescopes that are globally distributed in the southern hemisphere at the Siding Spring Observatory in Australia (KMTA), the Cerro Tololo Interamerican Observatory in Chile (KMTC), and the South African Astronomical Observatory in South Africa (KMST). Each KMTNet telescope is equipped with a camera, consisting of four 9k × 9k chips, yielding 4 deg<sup>2</sup> field of view. The event was found from the analysis of the data conducted after the 2016 season (Kim et al. 2018) and it was designated as KMT-2016-BLG-1089. Most KMTNet images were obtained in the  $I$  band and about one-tenth of images were obtained in the  $V$  band for the source color measurement. Thanks to the high-cadence coverage (1 hr<sup>−1</sup> for each telescope) using the multiple telescopes, the detailed structure of the light curve is well

<sup>20</sup> Besides this method, the nature of a wide-separation planet can be identified by several other methods. One method is detecting long-term bumps in the light curve caused by the primary star (Han et al. 2005). Another method is detecting the blended light from a host star by conducting high-resolution observations (Bennett & Rhie 2002). The last proposed method is conducting astrometric follow-up observations of isolated events using high-precision interferometers (Han 2006b).

**Table 1**  
Data Used in Analysis

Data Set	$N_{\text{data}}$	Range (HJD')
OGLE	154	7110.8–7659.6
KMTC	369	7500.7–7599.7
KMTS	575	7441.6–7675.3

**Note.**  $N_{\text{data}}$  indicates the number of each data set.  $\text{HJD}' \equiv \text{HJD} - 2450000$ .

delineated by the KMTNet data, despite the short duration of the event.

Reduction of the data is carried out using the photometry codes developed by the individual survey groups: Woźniak (2000) for the OGLE and Albrow et al. (2009) for the KMTNet data sets. These codes are based on the difference imaging method developed by Alard & Lupton (1998). For a subset of the KMTNet data sets, additional photometry is conducted using the pyDIA code (Albrow 2017) to measure the source color. The error bars of the individual data sets are readjusted according to the procedure described in Yee et al. (2012). We note that the KMTA data set is not used in the analysis because the photometry quality is relatively low and the data do not cover the major part of the light curve. In Table 1, we list the data sets used in the analysis along with numbers of data points,  $N_{\text{data}}$ , and the time ranges of the individual data sets.

### 3. Single-lens Single-source (1L1S) Modeling

In Figure 1, we present the light curve of OGLE-2016-BLG-1227. The light curve appears to be that of a 1L1S event affected by severe finite-source effects. We, therefore, start the analysis of the event by conducting a 1L1S modeling.

The modeling is carried out by searching for the lensing parameters that best describe the observed light curve. The light curve of a 1L1S event affected by finite-source effects is described by four lensing parameters. These parameters include the time of the closest lens-source approach,  $t_0$ , the lens-source separation at that time,  $u_0$ , the event timescale,  $t_E$ , and the normalized source radius,  $\rho$ . The normalized source radius is defined as the ratio of the angular source radius  $\theta_*$  to the angular Einstein radius, i.e.,  $\rho = \theta_*/\theta_E$ , and it is needed to describe the deformed light curve caused by finite-source effects. We search for the best-fit lensing parameters using the Markov Chain Monte Carlo (MCMC) method.

In computing finite-source magnifications, we consider the variation of the source surface brightness caused by limb darkening (Loeb & Sasselov 1995; Valls-Gabaud 1995; Witt 1995). To account for the limb-darkening variation, we model the surface brightness of the source star as

$$S_\lambda = \bar{S}_\lambda \left[ 1 - \Gamma_\lambda \left( 1 - \frac{3}{2} \cos \phi \right) \right], \quad (3)$$

where  $\bar{S}_\lambda$  denotes the mean surface brightness,  $\Gamma_\lambda$  is the linear limb-darkening coefficient, and  $\phi$  represents the angle between the line of sight toward the center of the source star and the normal to the source surface. The limb-darkening coefficient is determined based on the stellar type of the source star. As we will show in Section 5, the source is a bulge giant with a spectral type K3. Based on the stellar type, we set the limb-darkening coefficient as  $\Gamma_l = 0.41$  and  $\Gamma_v = 0.74$  by adopting the values from Claret (2000) under the assumption that

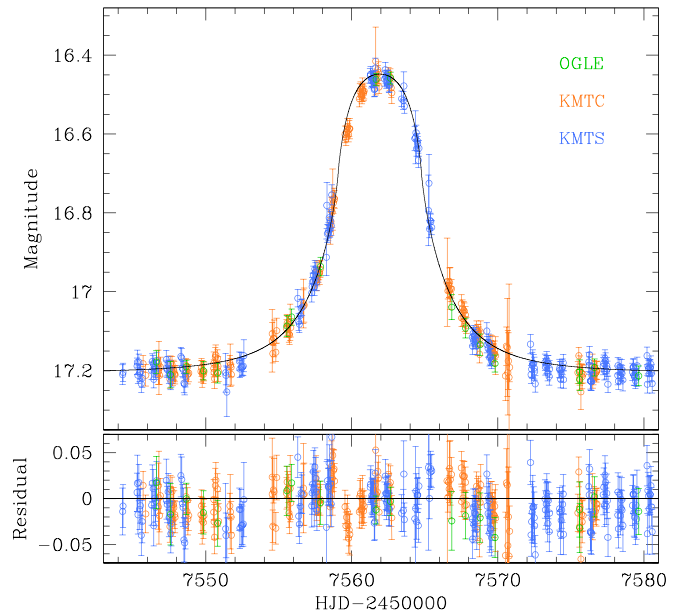


**Figure 1.** Light curve of OGLE-2016-BLG-1227. The curve drawn on the data points is the model obtained from the 1L1S fitting to the light curve considering finite-source effects.

$v_{\text{turb}} = 2 \text{ km s}^{-1}$ ,  $\log(g/g_\odot) = -2.4$ , and  $T_{\text{eff}} = 4500 \text{ K}$ . For the computation of finite-source magnifications, we use the semianalytic expressions derived by Gould (1994) and Witt & Mao (1994).

In Table 2, we present the best-fit lensing parameters obtained from the 1L1S modeling. In Figure 1, we also present the model curve superposed on the data points. We note that the estimated event timescale,  $t_E \sim 3.5$  days, is much shorter than those of typical lensing events with  $\sim(O)10$  days although events with such short timescales are not extremely rare. Furthermore, the normalized source radius,  $\rho \sim 1.05$ , is much bigger than typical values of  $\sim 0.01$ – $0.02$  for events involved with giant source stars. The unusually large  $\rho$  value suggests that the angular Einstein radius is likely to be very small. As we will show in Section 5, the angular radius of the source is  $\theta_* \sim 9.0 \mu\text{as}$ , and thus the angular Einstein radius of the event is  $\theta_E \sim 0.009 \text{ mas}$ . This is very much smaller than the  $\sim 0.5 \text{ mas}$  of typical lensing events. The very small values of  $t_E$  and  $\theta_E$  make the lens of the event a candidate of an FFP or a brown dwarf. We note that the lens of the event was originally found as a brown dwarf or an FFP candidate from the search for isolated events with short  $t_E$  and very small  $\theta_E$  conducted by Han et al. (2019), but the analysis is separately presented in this work for the reason presented in Section 4.

Although the observed light curve appears to be approximated by the 1L1S model, it is found that the solution leaves small residuals with an amplitude of  $\Delta I \lesssim 0.03 \text{ mag}$ . See the lower panel of Figure 1. The source was located close to the Moon during the lensing magnification and thus the photometry might have been affected by the light from the Moon. We check this possibility by conducting additional photometry for nearby stars. In Figure 2, we present the light curves of four nearby stars and compare them with that of the lensing event. It shows that the magnitudes of the comparison stars remain constant in contrast to the 1L1S residuals. This indicates that the photometry is not affected by the Moon and the residuals from the 1L1S solution are likely to be real.

**Table 2**  
Lensing Parameters

Parameter	1L1S	2L1S	
		Inner Solution	Outer Solution
$\chi^2$	1115.1	968.6	973.0
$t_0$ (HJD')	$7561.920 \pm 0.017$	$7561.999 \pm 0.031$	$7561.976 \pm 0.032$
$u_0$	$0.681 \pm 0.017$	$0.066 \pm 0.012$	$-0.057 \pm 0.012$
$t_E$ (days)	$3.54 \pm 0.05$	$45.37 \pm 8.07$	$52.23 \pm 12.76$
$t_{E,1}$ (days)	...	$4.05 \pm 0.06$	$4.01 \pm 0.06$
$t_{E,2}$ (days)	...	$45.19 \pm 8.09$	$52.07 \pm 12.79$
$s$	...	$3.68 \pm 0.21$	$3.57 \pm 0.24$
$q$	...	$124.48 \pm 46.79$	$168.99 \pm 98.86$
$\alpha$ (rad)	...	$4.783 \pm 0.062$	$4.689 \pm 0.066$
$\rho$	$1.05 \pm 0.013$	$0.092 \pm 0.017$	$0.080 \pm 0.018$
$t_{\text{eff}} =  u_0 t_E$ (days)	...	$3.00 \pm 0.08$	$2.97 \pm 0.08$
$t_* = \rho t_E$ (days)	...	$4.17 \pm 0.03$	$4.16 \pm 0.03$
$t_p = q^{-1/2}t_E$ (days)	...	$4.07 \pm 0.06$	$4.02 \pm 0.06$

**Note.** HJD' = HJD - 2450000. For the 2L1S solution,  $t_E$  represents the event timescale corresponding to the total mass of the binary lens, and  $t_{E,1}$  and  $t_{E,2}$  represent the timescales corresponding to the masses of individual lens components,  $M_1$  and  $M_2$ , respectively. The subscripts of the lens components are chosen according to the distances from the source trajectory. The source trajectory passes closer to the lower-mass lens component and thus  $M_1 < M_2$ ,  $t_{E,1} < t_{E,2}$ , and  $q = M_2/M_1 > 1$ .

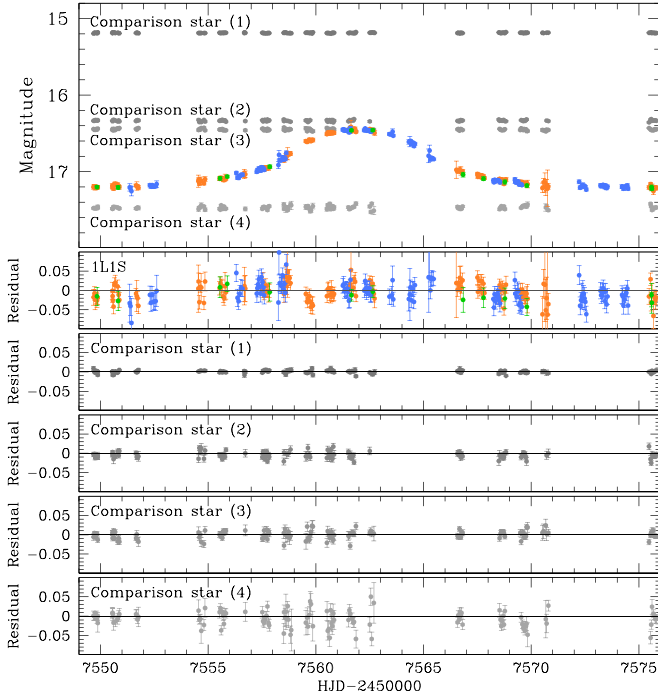


**Figure 2.** Comparison of the lensing light curve with those of four comparison stars around the lensing source. The lower four panels show the residuals of the comparison stars from baseline magnitudes and the second panel shows the residuals of the lensing event from the 1L1S solution.

#### 4. Binary-lens Single-source (2L1S) Modeling

Considering that the main part of the lensing light curve is produced by a planetary-mass object, we check whether there exists a host star located away from the planet. For this, we additionally conduct a 2L1S modeling of the light curve.

Compared to the 1L1S modeling, the 2L1S modeling requires three additional lensing parameters to describe the lens binarity. These parameters include the projected binary separation normalized to the angular Einstein radius,  $s$ , the mass ratio between the lens components,  $q = M_2/M_1$ , and the

angle between the binary axis and the source trajectory,  $\alpha$  (source trajectory angle).

In the 2L1S modeling, the solution of the lensing parameters is searched for in two steps. In the first step, we conduct a grid search for the parameters  $s$  and  $q$ , while the other parameters are searched for using the MCMC method. This procedure yields a  $\chi^2$  map on the  $s$ - $q$  parameter plane and we find local minima that appear in the map. In the second step, we refine the individual local minima by additionally conducting modeling with all parameters, including the grid parameters  $s$  and  $q$ , allowed to vary. We find a global solution by comparing the goodness of the local solutions. This procedure allows us to find degenerate solutions, if they exist.

We find that the model fit substantially improves with the introduction of an additional widely separated lens component  $M_2$ . The additional lens component has a mass much heavier than the lens component  $M_1$  responsible for the short magnified part of the light curve, suggesting that the additional lens component is the host of the planet. In Figure 3, we present both the 1L1S and 2L1S models and the residuals from the individual models. The solid curve superposed on the residuals of the 1L1S model in the middle panel represents the difference between the 1L1S and 2L1S models. It is found that the 2L1S residuals are substantially reduced relative to the 1L1S model. In Figure 4, we present the cumulative distribution of  $\Delta\chi^2 = \chi_{1L1S}^2 - \chi_{2L1S}^2$  between the 1L1S and 2L1S models to better show the region of the fit improvement. We find that the 2L1S improves the fit by  $\Delta\chi^2 \sim 146.5$ . We further check whether there is an additional weak long-term bump caused by the heavier companion, but we find no such bump. As we will show below, the reason for the absence of a bump is that the source passes nearly perpendicular to the binary axis.

The detection of the host star is based on the small deviations ( $\lesssim 0.03$  mag) with the timescale of several days around the peak of the event light curve. However, deviations with similar amplitudes and timescales could also arise due to the intrinsic variability of the source star and/or blending stars (if any). Therefore, we check the variability by comparing the baseline and the residuals from the 1L1S model during the event. The upper panel of Figure 5 shows the residuals from the 1L1S solution around the region of the lensing magnification and the

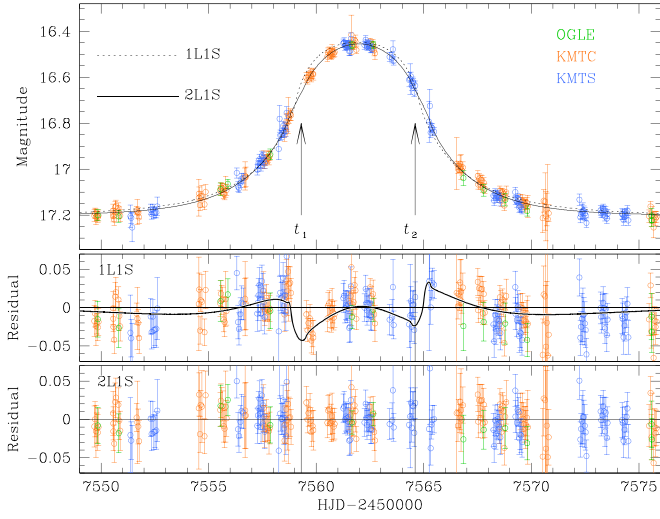


**Figure 3.** Comparison of the 1L1S (dotted curve) and 2L1S (solid curve) solutions. The middle and bottom panels show the residuals from the 1L1S and 2L1S solutions, respectively. The solid curve in the middle panel represents the difference between the 1L1S and 2L1S solutions. In the top panel, the arrows at  $t_1$  (HJD') = 7559.3 and  $t_2$  (HJD') = 7564.6 represent the times of the two dips in the residuals from the 1L1S solution.

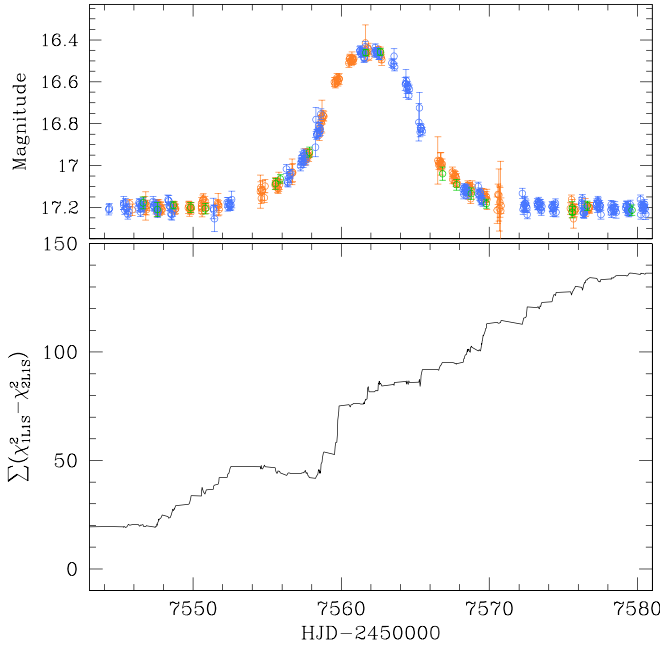


**Figure 4.** Cumulative distribution of  $\Delta\chi^2$  between the 1L1S and 2L1S models (lower panel). The light curve in the upper panel is presented to show the region of fit improvement.

lower panel shows the baseline during the same period of time as that of the above panel. We find that the standard deviation in the magnification region of  $\sigma_{\text{mag}} = 0.025$  mag is substantially bigger than the deviation in the baseline of  $\sigma_{\text{base}} = 0.016$  mag. This indicates that the observed signal is unlikely to be caused by the source or blend variability.

In searching for lensing solutions, we find that the observed light curve is subject to the so-called inner/outer degeneracy. This degeneracy arises because the planetary anomalies produced by the source approaching the inner and outer sides (with respect to the host of the planet) of the planetary caustic are similar to each other (Gaudi & Gould 1997). It is found that

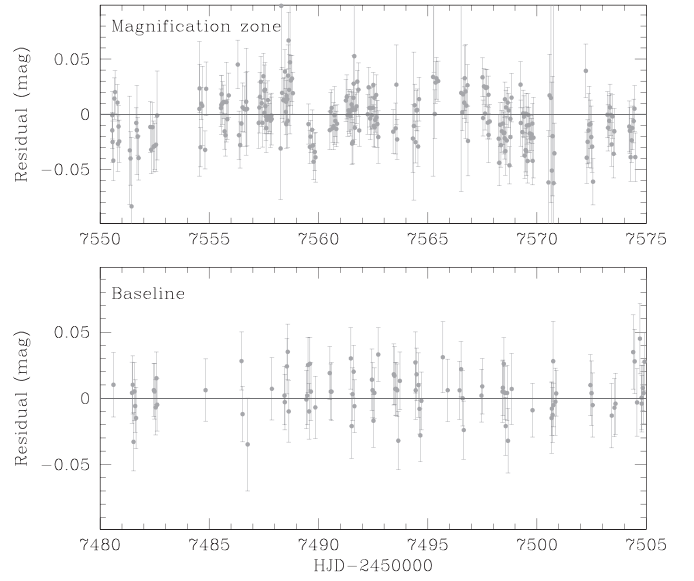


**Figure 5.** Comparison of the residuals from the 1L1S solution around the region of the lensing magnification (upper panel) and the baseline (lower panel).

the degeneracy is severe although the inner solution is slightly preferred over the outer solution by  $\Delta\chi^2 \sim 4.3$ .

In Table 2, we list the best-fit lensing parameters of the 2L1S solutions for both the inner and outer solutions. For each solution, we present three values of timescales ( $t_E$ ,  $t_{E,1}$ ,  $t_{E,2}$ ), in which  $t_E$  represents the event timescale corresponding to the total mass of the binary lens, and  $t_{E,1} = [1/(1+q)]^{1/2}t_E$  and  $t_{E,2} = [q/(1+q)]^{1/2}t_E$  represent the timescales corresponding to the masses of individual lens components,  $M_1$  and  $M_2$ . We note that the subscripts of the lens components  $M_1$  and  $M_2$  are chosen according to the distances from the source trajectory. The source trajectory approaches closer to the lower-mass lens component and thus  $M_1 < M_2$ ,  $t_{E,1} < t_{E,2}$ , and  $q = M_2/M_1 > 1$ . The estimated mass ratio between the lens components,  $q \sim 124$  for the inner solution and  $q \sim 169$  for the outer solution, is much bigger than unity, indicating that  $M_2$  is the host of the planet  $M_1$ . The host is separated from the planet with a projected separation of  $s \sim 3.6$ .

In Figure 6, we present the lens-system configurations of the inner and outer 2L1S solutions. The upper panel shows the whole view including both lens components. The lower two panels show the zoom of the region around the planetary caustic for the inner (right panel) and outer (left panel) solutions. The three brown circles in the lower panels represent the source positions at three different times of  $t_0$ ,  $t_1$ , and  $t_2$ . The time  $t_0$  corresponds to the time of the closest source approach to the planetary caustic, and the times  $t_1$  (HJD') = 7559.3 and  $t_2$  (HJD') = 7564.6 correspond to the times of the two dips in the residuals from the 1L1S model. See the corresponding times  $t_1$  and  $t_2$  marked in Figure 3. The size of the circles is scaled to the source size. It is found that the source is much bigger than the caustic. This causes severe attenuation of the signal induced by the caustic and makes the light curve appear to be very similar to that of a 1L1S event.

We note that the estimated lensing parameters have large uncertainties. See Table 2. The main reason for the large uncertainties of the lensing parameters is that the observed lensing magnification is mostly produced by the planet, and the planet's host is characterized by the subtle deviations in the

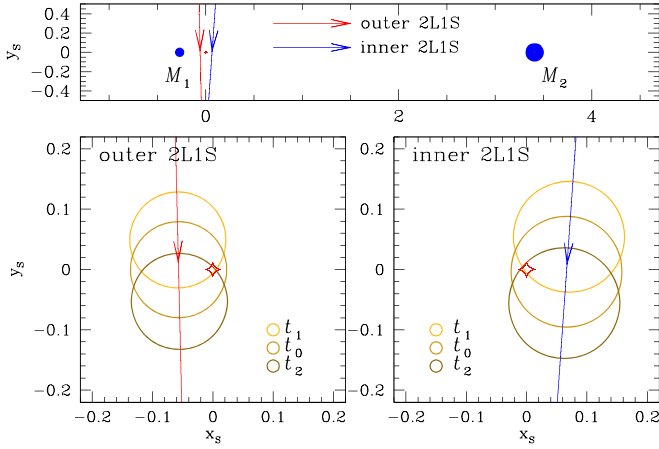


**Figure 6.** Lens-system configurations of the inner and outer 2L1S solutions. Coordinates are centered at the center of the planetary caustic. The time  $t_0$  is the time of the closest source approach to the planetary caustic, and the times  $t_1$  and  $t_2$  correspond to the times of the two dips in the residuals from the 1L1S model presented in Figure 4. In each panel, the line with an arrow represents the source trajectory. The circles on the source trajectory in the two lower panels represent the source positions at  $t_0$ ,  $t_1$ , and  $t_2$ . The size of the circle is scaled to the source size.

planet-induced magnifications. In this case, the uncertainty of the timescale  $t_E \sim t_{E,2}$  is large. The large uncertainty of  $t_E$  propagates into the uncertainty of the mass ratio because the mass ratio is related to the timescale by  $q = (t_{E,1}/t_{E,2})^{1/2} \sim (t_{E,1}/t_E)^{1/2}$ . The uncertain timescale also induces large uncertainties of  $u_0$  and  $\rho$  because the measured source-crossing duration results from the combination of these parameters by  $2(\rho^2 - u_0^2)^{1/2}t_E$ .

In Figure 7, we present the  $\Delta\chi^2$  distributions of points in the MCMC chain on the  $t_{\text{eff}}-t_*-t_p$  parameter planes. The individual timescales represent  $t_{\text{eff}} = |u_0|t_E$ ,  $t_* = \rho t_E$ , and  $t_p = q^{-1/2}t_E$ , respectively. The effective timescale,  $t_{\text{eff}}$ , is frequently used because it facilitates intuitive understanding of a light curve independent of separately determining  $u_0$  and  $t_E$  from modeling. The source-crossing timescale,  $t_*$ , represents an approximate timescale for the lens to transit the source surface.<sup>21</sup> Finally, the planet timescale,  $t_p$ , denotes an approximate timescale of the isolated event produced by the planet. We present the estimated values of these timescales in Table 2. These timescales are derived from the shape of a lensing light curve, and thus they are tightly constrained despite the large uncertainties of the lensing parameters, as demonstrated in Figure 7.

## 5. Angular Einstein Radius

We determine the angular Einstein radius from the normalized source radius  $\rho$  together with the angular source radius  $\theta_*$  by  $\theta_E = \theta_*/\rho$ . The normalized source radius is determined from modeling the light curve. For the estimation of the angular source radius, we use the method of Yoo et al. (2004). According to this method, we first place the source position in the instrumental color–magnitude diagram (CMD) of stars around the source. We then measure the offsets in color,  $\Delta(V-I)$ , and magnitude,  $\Delta I$ , of the source from the centroid of the red giant clump (RGC) in the CMD. With the measured offsets  $\Delta(V-I)$  and  $\Delta I$  combined with the known

<sup>21</sup> The exact expression for the source-crossing timescale, i.e., half of the duration for the lens to stay on the source surface, is  $t_* = (\rho^2 - u_0^2)^{1/2}t_E$ .

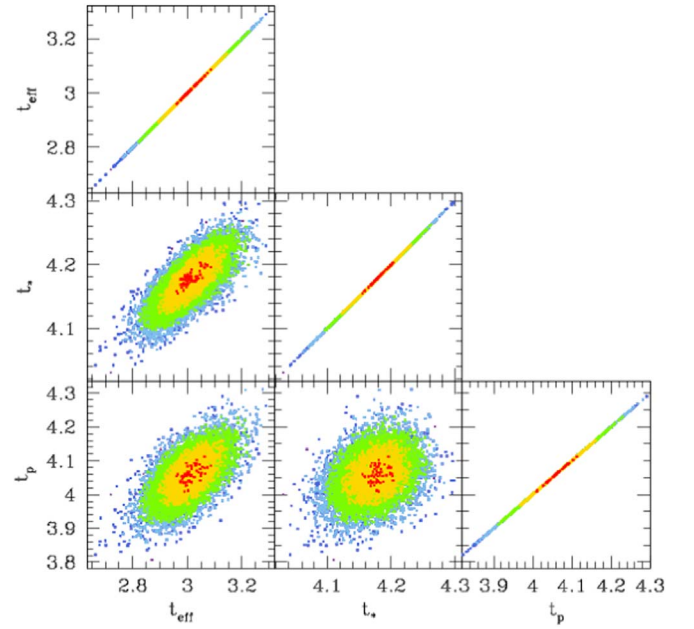


**Figure 7.**  $\Delta\chi^2$  distributions of points in the MCMC chain on the parameter planes of the  $(t_{\text{eff}}, t_*, t_p)$  combinations. The red, yellow, green, and blue colors represent points with  $1\sigma$ ,  $2\sigma$ ,  $3\sigma$ , and  $4\sigma$ , respectively. The distributions are constructed based on the inner 2L1S solution.

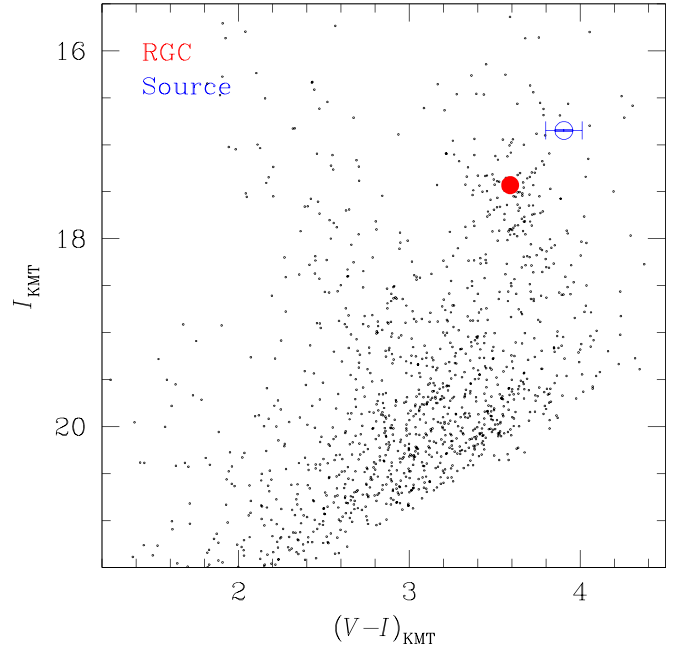


**Figure 8.** Source location (blue empty circle) with respect to the centroid of red giant clump (RGC, red dots) in the instrumental color–magnitude diagram constructed based on the pyDIA photometry of the KMTC data set.

dereddened source color and magnitude of the RGC centroid,  $(V-I, I)_{\text{RGC},0} = (1.06, 14.65)$  (Bensby et al. 2013; Nataf et al. 2013), the dereddened color and magnitude of the source are estimated by

$$(V-I, I)_0 = (V-I, I)_{\text{RGC},0} + \Delta(V-I, I). \quad (4)$$

In Figure 8, we present the positions of the source and the RGC centroid in the instrumental CMD. The CMD is constructed using the pyDIA photometry of the KMTC data set. We note that the location of the blend cannot be determined

**Table 3**  
Angular Einstein Radius and Relative Lens-source Proper Motion

Parameter	Inner Solution	Outer Solution
$\theta_E$ (mas)	$0.098 \pm 0.044$	$0.113 \pm 0.058$
$\theta_{E,1}$ (mas)	$0.007 \pm 0.003$	$0.009 \pm 0.004$
$\theta_{E,2}$ (mas)	$0.097 \pm 0.043$	$0.112 \pm 0.057$
$\mu$ (mas yr <sup>-1</sup> )	$0.79 \pm 0.10$	$0.79 \pm 0.10$

**Note.** The Einstein radius  $\theta_E$  corresponds to the total mass of the lens  $M = M_1 + M_2$ , and  $\theta_{E,1}$  and  $\theta_{E,2}$  represent the Einstein radii corresponding to  $M_1$  and  $M_2$ , respectively.

because the baseline flux is dominated by the source flux and the flux from the blend is consistent with zero within the photometry uncertainty. The color and magnitude of the source in the instrumental CMD are  $(V - I, I) = (3.91 \pm 0.11, 16.85 \pm 0.01)$  compared to those of the RGC centroid of  $(V - I, I)_{\text{RGC}} = (3.59, 17.43)$ . With the measured offsets of  $\Delta(V - I) = 0.32 \pm 0.11$  and  $\Delta I = 0.58 \pm 0.01$ , the dereddened color and brightness of the source are estimated as  $(V - I, I)_0 = (1.38 \pm 0.11, 14.07 \pm 0.01)$ . The estimated source color and brightness indicate that the source is a typical bulge giant with a spectral type K3.

Once the dereddened color and magnitude are determined, we then estimated the angular source radius. For this, we first convert the  $V - I$  color into  $V - K$  color using the color-color relation of Bessell & Brett (1988) and then the angular source radius is estimated using the Kervella et al. (2004) relation between  $V - K$  and  $\theta_*$ . This procedure yields an angular source radius of

$$\theta_* = 9.01 \pm 1.15 \text{ } \mu\text{as.} \quad (5)$$

With the measured angular source radius, the angular Einstein radius is estimated as

$$\theta_E = \frac{\theta_*}{\rho} = \begin{cases} 0.098 \pm 0.044 \text{ mas} & \text{(inner solution),} \\ 0.113 \pm 0.058 \text{ mas} & \text{(outer solution).} \end{cases} \quad (6)$$

The estimated relative lens-source proper motion is

$$\mu = \frac{\theta_E}{t_E} = 0.79 \pm 0.10 \text{ mas yr}^{-1} \quad (7)$$

for both the inner and outer solutions. We note that the fractional uncertainty of the relative lens-source proper motion,  $\sigma_\mu/\mu \sim 13\%$ , is substantially smaller than the uncertainty of the angular Einstein radius,  $\sigma_{\theta_E}/\theta_E \sim 50\%$ . This is because the proper motion in the lensing modeling is computed by  $\mu \sim \theta_*/t_*$  and the uncertainty of the source-crossing timescale  $t_*$  is significantly smaller than the uncertainty of the event timescale  $t_E$ .

In Table 3, we summarize the estimated Einstein radii and relative lens-source proper motions for the inner and outer solutions. Also presented are the angular Einstein radii corresponding to the masses of the individual lens components,  $\theta_{E,1}$ , and  $\theta_{E,2}$ , similar to the presentation of  $t_{E,1}$  and  $t_{E,2}$  in Table 2. We note that the estimated  $\theta_{E,1} \sim 0.007\text{--}0.009$  mas is consistent with the Einstein radius estimated from the 1L1S modeling. We also note that the measured angular Einstein radius,  $\theta_E \sim 0.1$  mas, is substantially smaller than  $\sim 0.5$  mas of a typical lensing event produced by a low-mass star with a mass of  $\sim 0.3 M_\odot$  located roughly halfway between the observer and the bulge source. The angular Einstein radius is

related to the lens mass and distance by Equation (1). Then, the small angular Einstein radius suggests that the lens has a small mass and/or it is located close to the source.

## 6. Physical Lens Parameters

For the unique determinations of the physical lens parameters of the lens mass  $M$  and distance  $D_L$ , one must measure both the angular Einstein radius and the microlens parallax  $\pi_E$ , i.e.,

$$M = \frac{\theta_E}{\kappa\pi_E}; \quad D_L = \frac{\text{au}}{\pi_E\theta_E + \pi_S}. \quad (8)$$

Here  $\pi_S = \text{au}/D_S$  represents the parallax of the source. For OGLE-2016-BLG-1227, the angular Einstein radius is measured from the obvious finite-source effects, but the microlens parallax cannot be measured due to the short timescale of the observed light curve, i.e.,  $t_{E,1}$ . We, therefore, estimate  $M$  and  $D_L$  by conducting a Bayesian analysis of the event based on the measured event timescale  $t_E$  and the relative lens-source proper motion  $\mu$ . We use  $\mu$  instead of  $\theta_E$  because  $t_E$  and  $\theta_E$  are highly correlated.

In the Bayesian analysis, we conduct a simulation of Galactic lensing events using the prior models of the mass function of astronomical objects in the Galaxy and their physical and dynamical distributions. For the mass function, we consider both stellar and remnant lenses, i.e., black holes, neutron stars, and white dwarfs, by adopting the Chabrier (2003) model and the Gould (2000) model for the mass functions of stars and remnants, respectively. In the simulation, lenses and source stars are located following the physical distribution model of Han & Gould (2003) and their motions are computed using the dynamical model of Han & Gould (1995). We produce  $10^7$  artificial lensing events, from which the probability distributions of  $M$  and  $D_L$  are obtained with the constraints of the measured  $t_E$  and  $\mu$ .

In Figure 9, we present the probability distributions of the lens mass of the host star ( $M_{\text{host}}$ , upper panel) and the lens-source separation ( $D_{\text{LS}}$ , lower panel) obtained from the Bayesian analysis. As indicated by the small angular Einstein radius, the lens is estimated to lie close to the source, and thus we present the distribution of  $D_{\text{LS}}$  instead of  $D_L$ . To check the importance of the  $\mu$  constraint, we present two sets of distributions obtained with the combined  $\mu$  and  $t_E$  constraint (solid curves) and with only the  $t_E$  constraint (dotted curves). The distributions show that the lens mass estimated with the additional  $\mu$  constraint is substantially lower and the lens-source separation is smaller than those estimated with the single  $t_E$  constraint. This indicates that the measured  $\mu$  provides an important constraint on the physical lens parameters.

In Table 4, we list the estimated physical lens parameters. We note that both the inner and outer 2L1S solutions result in similar parameters, and thus we present the parameters based on the inner 2L1S solution. The presented parameters are the median values of the Bayesian distributions, and the upper and lower limits correspond to the 15.9% and 84.1% of the distributions. It is found that the lens is a planetary system composed of a giant planet and a low-mass host star. The masses of the planet and host are

$$M_p = 0.79_{-0.39}^{+1.30} M_J \quad (9)$$

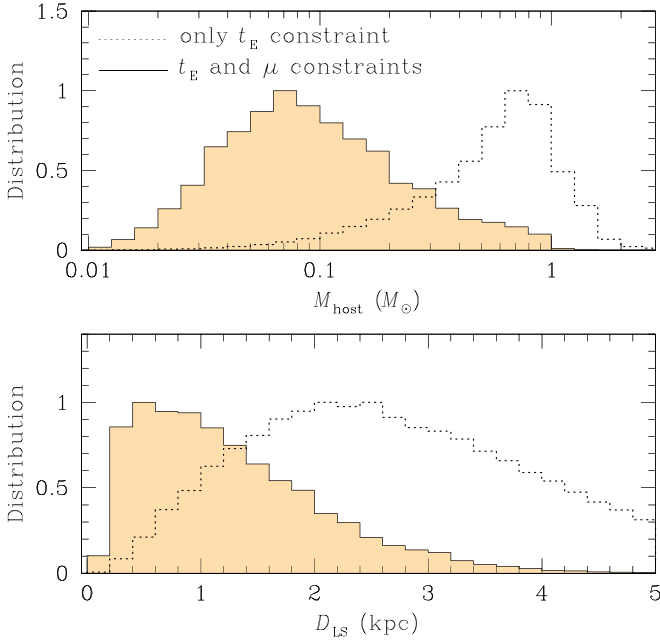


**Figure 9.** Probability distributions of the lens mass ( $M_{\text{host}}$ ) and the lens-source separation ( $D_{\text{LS}}$ ) obtained from the Bayesian analysis. The solid curve is the distribution obtained with the combined  $\theta_E$  and  $t_E$  constraint and the dotted curve is the distribution obtained with only the  $t_E$  constraint.

**Table 4**  
Physical Lens Parameters

Parameter	Constraint	
	$t_E + \theta_E$	$t_E$ only
$M_p (M_J)$	$0.79^{+1.30}_{-0.39}$	$4.98^{+3.05}_{-2.94}$
$M_{\text{host}} (M_{\odot})$	$0.10^{+0.17}_{-0.05}$	$0.68^{+0.42}_{-0.41}$
$D_{\text{LS}} (\text{kpc})$	$1.21^{+0.96}_{-0.63}$	$2.60^{+1.29}_{-1.13}$
$a_{\perp} (\text{au})$	$3.4^{+2.1}_{-1.0}$	$11.5^{+3.1}_{-4.3}$

**Note.** The presented parameters are the median values of the Bayesian distributions, and the upper and lower limits correspond to the 15.9% and 84.1% of the distributions.

and

$$M_{\text{host}} = 0.10^{+0.17}_{-0.05} M_{\odot}, \quad (10)$$

respectively. The planetary system is located in the bulge with a line-of-sight separation from the source star of

$$D_{\text{LS}} = 1.21^{+0.96}_{-0.63} \text{ kpc}. \quad (11)$$

The planet and host are separated in projection by

$$a_{\perp} = 3.4^{+2.1}_{-1.0} \text{ au}. \quad (12)$$

Considering that the snowline of the system is  $a_{\text{sl}} \sim 2.7 \text{ au} (M_{\text{host}}/M_{\odot}) \sim 0.4 \text{ au}$ , the planet is a wide-separation planet located well beyond the snowline of the host star.

## 7. Discussion and Conclusion

We analyzed the microlensing event OGLE-2016-BLG-1227, for which the event timescale was short and the light curve was affected by severe finite-source effects. The light curve appeared to be that of a 1L1S event and the analysis

based on the 1L1S interpretation yielded a short timescale and a very small angular Einstein radius, suggesting that the lens could be an FFP. From the close inspection of the small residuals from the 1L1S solution, we found that the residual was explained by the existence of an additional widely separated heavier lens component, indicating that the lens was a planetary system with a wide-separation planet rather than an FFP. From the Bayesian analysis with the constraints of the measured event timescale and relative lens-source proper motion, we estimated that the lens was composed of a planet with a mass of  $M_p = 0.79^{+1.30}_{-0.39} M_J$  and a host star with a mass of  $M_{\text{host}} = 0.10^{+0.17}_{-0.05} M_{\odot}$ . It turned out that the planet was located well beyond the snowline of the host with a projected separation of  $a_{\perp} = 3.4^{+2.1}_{-1.0} \text{ au}$ . It was estimated that the lens was located close to the source with a lens-source separation of  $D_{\text{LS}} = 1.21^{+0.96}_{-0.63} \text{ au}$ .

The event demonstrates that detecting deviations from 1L1S light curves provides an important method to distinguish wide-separation planets from FFPs. Besides OGLE-2016-BLG-1227, there were two planetary events, in which planets were detected through isolated events and their widely separated hosts were identified in lensing light curves. The first case is MOA-bin-1 (Bennett et al. 2012). For this event, the lensing light curve exhibited little lensing magnification attributable to the host of the planet similar to OGLE-2016-BLG-1227, but the planetary signal was entirely due to a brief caustic feature. The second case is OGLE-2008-BLG-092 (Poleski et al. 2014). For this event, the planet was detected through the isolated event channel, but in this case the host of the planet was on the source trajectory, and gave rise to a bump in the lensing light curve. OGLE-2016-BLG-1227 shows that there is a range of deviations in the signatures of host stars and that it is possible to identify the existence of a host even when a deviation is subtle.

Due to the unusual nature of OGLE-2016-BLG-1227, in which the relative lens-source proper motion  $\mu = \theta_E/t_E$  is well determined, but the separate values of  $\theta_E$  and  $t_E$  are poorly constrained, the information that can be obtained from high-resolution follow-up observations would be different from that of normal events. If follow-up observations are conducted to normal events with well-estimated  $\theta_E$ , the flux from the host is measured and from this one can make a diagram of the predicted host flux in the  $M$ - $D_L$  plane. Comparison of this diagram to the  $\theta_E$  constraint in the same  $M$ - $D_L$  plane will allow one to determine  $M$  and  $D_L$  from the intersection of these two constraints, e.g., Yee (2015) and Fukui et al. (2019). Even if  $\theta_E$  is not known because of poor  $\rho$  measurement, the event timescale  $t_E$  is known. Then, from late time follow-up imaging conducted when the source and lens are separated, one can measure the lens-source separation  $\Delta\theta$  and therefore the relative lens-source proper motion can be estimated by  $\mu = \Delta\theta/\Delta t$ , from which the angular Einstein radius is estimated by  $\theta_E = \mu t_E$ . Here  $\Delta t$  represents the difference between the time of follow-up observation and  $t_0$ .

For events with a well-measured  $\mu$  but with uncertain values of  $\theta_E$  and  $t_E$ , the time of follow-up observations can be predicted. If a follow-up observation is conducted using the European Extremely Large Telescope with an aperture of 39 m, the FWHM in the  $J$  and  $H$  bands would be  $\text{FWHM}(J) \sim 7.1 \text{ mas}$  and  $\text{FWHM}(H) \sim 10.3 \text{ mas}$ , respectively. Assuming that the lens and source can be resolved when they are separated by  $\sim 1.5 \times \text{FWHM}$ , the required times for the

resolution would be  $\Delta t \sim 13.5$  yr and  $\sim 19.6$  yr from  $J$  and  $H$  imaging observations, respectively. These correspond to the years 2028 and 2035, respectively. With a resolved host star, its distance  $D_L$  and mass  $M_{\text{host}}$  would be constrained from the color and flux.

However, this does not necessarily imply that the planet mass  $M_p = M_{\text{host}}/q$  can also be well determined because the mass ratio is poorly known. If one can estimate  $M_{\text{host}}$  and  $D_L$  from the  $J$  and  $H$  color and magnitude, then there will be two possible cases. If the lens is in the disk, one can estimate  $\pi_{\text{rel}} = \text{au}(D_L^{-1} - D_S^{-1})$ , where  $D_S \sim 9$  kpc. Then the Einstein radius can be determined by the relation in Equation (1), although uncertainty will be fairly large because  $M_{\text{host}}$  and  $D_L$  are somewhat uncertain together with the uncertainty of the source distance. If the lens is in the bulge, in contrast, it will be difficult to estimate  $\theta_E$  any better than from the microlensing data. This will cause  $q$  and  $M_p$  to be poorly constrained.

Work by C.H. was supported by the grants of National Research Foundation of Korea (2017R1A4A1015178 and 2019R1A2C2085965). Work by A.G. was supported by US NSF grant AST-1516842 and by JPL grant 1500811. A.G. received support from the European Research Council under the European Union's Seventh Framework Programme (FP 7) ERC Grant Agreement No. [32103]. The OGLE project has received funding from the National Science Centre, Poland, grant MAESTRO 2014/14/A/ST9/00121 to A.U. This research has made use of the KMTNet system operated by the Korea Astronomy and Space Science Institute (KASI) and the data were obtained at three host sites of CTIO in Chile, SAAO in South Africa, and SSO in Australia. Work by R.P. was partly supported by Polish National Agency for Academic Exchange grant Polish Returns 2019. We acknowledge the high-speed internet service (KREONET) provided by Korea Institute of Science and Technology Information (KISTI).

#### ORCID iDs

Cheongho Han  <https://orcid.org/0000-0002-2641-9964>  
 Michael D. Albrow  <https://orcid.org/0000-0003-3316-4012>  
 Sun-Ju Chung  <https://orcid.org/0000-0001-6285-4528>  
 Kyu-Ha Hwang  <https://orcid.org/0000-0002-9241-4117>  
 Yoon-Hyun Ryu  <https://orcid.org/0000-0001-9823-2907>  
 In-Gu Shin  <https://orcid.org/0000-0002-4355-9838>  
 Yossi Shvartzvald  <https://orcid.org/0000-0003-1525-5041>  
 Jennifer C. Yee  <https://orcid.org/0000-0001-9481-7123>  
 Weicheng Zang  <https://orcid.org/0000-0001-6000-3463>

Richard W. Pogge  <https://orcid.org/0000-0003-1435-3053>  
 Chun-Hwey Kim  <https://orcid.org/0000-0001-8591-4562>  
 Woong-Tae Kim  <https://orcid.org/0000-0003-4625-229X>  
 Jan Skowron  <https://orcid.org/0000-0002-2335-1730>  
 Paweł Pietrukowicz  <https://orcid.org/0000-0002-2339-5899>  
 Krzysztof Ulaczyk  <https://orcid.org/0000-0001-6364-408X>

#### References

- Alard, C., & Lupton, R. H. 1998, *ApJ*, 503, 325  
 Albrow, M. 2017, MichaelDAIbrow/pyDIA: Initial Release on Github, Version v1.0.0, Zenodo, doi:10.5281/zenodo.268049  
 Albrow, M., Horne, K., Bramich, D. M., et al. 2009, *MNRAS*, 397, 2099  
 Bennett, D. P., & Rhie, S. H. 2002, *ApJ*, 574, 985  
 Bennett, D. P., Sumi, T., Bond, I. A., et al. 2012, *ApJ*, 757, 119  
 Bensby, T., Yee, J. C., Feltzing, S., et al. 2013, *A&A*, 549, 147  
 Bessell, M. S., & Brett, J. M. 1988, *PASP*, 100, 1134  
 Chabrier, G. 2003, *ApJL*, 586, L133  
 Claret, A. 2000, *A&A*, 363, 1081  
 Fukui, A., Suzuki, D., & Koshimoto, N. 2019, *AJ*, 158, 206  
 Gaudi, B. S., & Gould, A. 1997, *ApJ*, 486, 85  
 Gould, A. 1994, *ApJL*, 421, L71  
 Gould, A. 1997, *ApJ*, 480, 188  
 Gould, A. 2000, *ApJ*, 535, 928  
 Gould, A., & Loeb, A. 1992, *ApJ*, 396, 104  
 Gould, A., Udalski, A., Monard, B., et al. 2009, *ApJL*, 698, L147  
 Han, C. 2006a, *ApJ*, 638, 1080  
 Han, C. 2006b, *ApJ*, 644, 1232  
 Han, C., Chung, S.-J., Kim, D., et al. 2004, *ApJ*, 604, 372  
 Han, C., Gaudi, B. S., An, J. H., & Gould, A. 2005, *ApJ*, 618, 962  
 Han, C., & Gould, A. 1995, *ApJ*, 447, 53  
 Han, C., & Gould, A. 2003, *ApJ*, 592, 172  
 Han, C., & Kang, Y. W. 2003, *ApJ*, 596, 1320  
 Han, C., Lee, C.-U., Udalski, A., et al. 2019, *AJ*, in press  
 Kervella, P., Thévenin, F., Di Folco, E., & Ségransan, D. 2004, *A&A*, 426, 29  
 Kim, D.-J., Kim, H.-W., Hwang, K.-H., et al. 2018, *AJ*, 155, 76  
 Kim, S.-L., Lee, C.-U., Park, B.-G., et al. 2016, *JKAS*, 49, 37  
 Loeb, A., & Sasselov, D. 1995, *ApJL*, 449, L33  
 Mao, S., & Paczyński, B. 1991, *ApJL*, 374, L37  
 Mróz, P., Ryu, Y.-H., Skowron, J., et al. 2018, *AJ*, 155, 121  
 Mróz, P., Udalski, A., Bennett, D. P., et al. 2019, *A&A*, 622, A201  
 Nataf, D. M., Gould, A., Fouqué, P., et al. 2013, *ApJ*, 769, 88  
 Poleski, R., Skowron, J., Udalski, A., et al. 2014, *ApJ*, 795, 42  
 Refsdal, S. 1966, *MNRAS*, 134, 315  
 Udalski, A., Szymański, M. K., & Szymański, G. 2015, *Acta Astron*, 65, 1  
 Valls-Gabaud, D. 1995, in *Large Scale Structure in the Universe*, ed. J. P. Mücke, S. Gottlöber, & V. Müller (Singapore: World Scientific), 326  
 Witt, H. J. 1995, *ApJ*, 449, 42  
 Witt, H. J., & Mao, S. 1994, *ApJ*, 430, 50  
 Woźniak, P. R. 2000, *AcAau*, 50, 421  
 Yee, J. C. 2015, *ApJL*, 814, L11  
 Yee, J. C., Shvartzvald, Y., Gal-Yam, A., et al. 2012, *ApJ*, 755, 102  
 Yoo, J., DePoy, D. L., Gal-Yam, A., et al. 2004, *ApJ*, 603, 139